Physics of Complex Systems Master Thesis

Phase Separation of Active Fluids on a Substrate

Supervisors:
Andrea Antonio Gamba
Cesare Nardini

Candidate:
Nicolò Angeli

July 2025

Abstract

Active systems are inherently out-of-equilibrium, and examples range both synthetic and natural systems, especially encountered in biological contexts. Due to these energy fluxes, active systems often display phenomenologies that are impossible at equilibrium as for example phase separation in the presence of mass currents in the steady state. In this work, we study phase separating active systems taking into account that particles move in a low-Reynolds number fluid. We aim at addressing an aspect often overlooked in standard theoretical formulations: momentum dissipation due to interactions with the substrate; in fact most experimental setups operate in quasi-two-dimensional geometries where the substrate or confining walls act as a momentum sink, effectively introducing friction into the system's hydrodynamics. Yet the theoretical studies so far concentrated in describing either the fully wet (momentum exactly conserved) or fully dry (fluid velocity not being present) limits. We study the intermediate case where the fluid is present but momentum is not conserved within a field-theoretical appraoch. Starting from Active Model H[1], a model where the order parameter ϕ is coupled to a momentum-conserving fluid, we incorporate the friction through a term in the Navier-Stokes equation that breaks momentum conservation, similarly to [2]. Our central findings reveals that interfaces can be unstable even with the addition of friction. We establish that this instability is governed by a critical threshold on activity strength, below this threshold, interfaces become unstable to linear perturbations (capillary waves), this instability leads fundamentally to microphase separation. Through linear stability analysis, we derived an expression for the growth rate of interface perturbations. In the high friction limit, our model effectively reduces to the dynamics characteristic of Model B (a model without hydrodynamic couplings). Conversely, in the low friction regime, it recovers the dynamics observed in the Active Model H without friction. Finally, to validate our theoretical predictions, we conducted extensive numerical simulations using pseudo-spectral methods, these simulations consistently confirmed the existence of the predicted critical activity threshold across a wide range of parameter sets.

Contents

Appendix

1. Introduction

Phase separation is a fundamental phenomenon in nature, presenting itself in very different systems from synthetic materials to cell biology. This phenomenon describes the spontaneous demixing of a homogeneous mixture into distinct, coexisting phases with different compositions or densities. While equilibrium phase separation is understood through standard thermodynamics, where systems evolve to minimize their free energy, an increasing attention was recently devoted to describe many phase-separating systems operating far from equilibrium, particularly in biological contexts [3].
This report addresses phase separation out of equilibrium, where a free energy cannot be defined, with a specific focus on how the presence of the fluid in which particles move modifies its phenomenology; this is a key question for experiments, because most active particles self-propel in a fluid but also close to a substrate or in geometries that imply momentum exchange between the (active) fluid and the outer environment.

Classical phase separation, studied in passive systems, is driven by the free energy minimization, leading to well-understood phenomena such as spinodal decomposition, where a homogeneous mixture becomes unstable to small fluctuations, creating interconnected domains; and Ostwald ripening, where larger domains grow at the expense of smaller ones [4], [5]. Moreover, the field-theoretical framework was successful in describing universal features of phase separation dynamics. In particular continuum models with a conserved order parameter, such as Model B (without hydrodynamics) and Model H (with hydrodynamics) [5], are excellent tools for predicting coarsening laws, interfacial dynamics and pattern formation.
On the other hand, active systems introduce a variety of new phenomena. Active particles continuously consume energy to generate motion and forces [6], the input of energy at the microscopic scale breaks time-reversal symmetry and precludes the existence of equilibrium states. For example, activity can induce phase separation even in the absence of attractive interaction, a phenomenon known as motility-induced phase separation.
The influence of activity extends beyond this basic mechanism, driving a rich phenomenology at the macroscopic level. Activity can lead to phase separation in different forms, for example microphase separation, bubbly phase separation and active foams, as observed in Active odel B+ [3], [7], [8]. These tree states differ by the shape of the domains, going from numerous bubbles of one phase immersed in the other one, to interconnected domains forming network like structure in active foams.
Activity also facilitates the formation of biomolecular condensates through liquid-liquid phase separation [9], and provides insights into chromosome positioning through activity-based segregation [10]. Interestingly, active systems also apply to larger scales, influencing pattern formation in nutrient-poor ecologies [11] and offering insights into human demographics, such as segregation patterns [12].

In this work we take a field-theoretical approach to the study of phase separation in active systems. This framework builds on passive models, incorporating terms that break detailed balance such as active forces on the fluid. However a critical gap exists between theoretical models and experiments, as most theoretical studies focus on fully dry (no hydrodinamics) or fully wet systems, where the fluid is idealized and interactions with the substrate are ignored. Whereas usual active matter realizations occur in quasi-two-dimensional geometries where interactions between boundaries and particles, or between boundaries and the fluid in which particles are immersed, become relevant. Examples include bacterial colonies on surfaces [13], microtubule bundles confined in narrow geometries [14] and cell monolayers on substrates [15].

This report addresses this gap by studying an extension Active Model H that includes friction, proposed in [2]. This in particular happens either when there is a direct momentum exchange with the substrate or in quasi-two-dimensional systems with no-slip walls, when the vertical direction is averaged out. Our primary goal is to understand how friction modifies its phase separation kinematics, particularly focusing on interfacial stability. We begin by reviewing passive phase separation, describing the relevant field models (Model B and Model H [5]) and the key mechanisms (chapter 2); then we introduce activity through Active Model H [1], explaining how active stress modify the phase separation dynamics (chapter 3). Finally we present our result on Active Model H with friction, including linear stability analysis of capillary waves and numerical simulations (chapter 4). We found that binodals and Ostwald ripening reduce to Model B dynamics, but interface stability is affected by friction. Unlike frictionless Active Model H, where contractile activity is enough to destabilize interfaces, friction introduces a threshold on the activity that determines the stability. Moreover this shows that the instability shape is fundamentally driven by capillary waves.

2. Passive Phase Separation

This chapter reviews key concepts of phase separation in passive systems, which provide the theoretical foundation for understanding active phase separation. We begin with the thermodynamic framework based on free energy minimization. We focus on systems with a conserved order parameter ϕ, whose total amount doesn't change with the evolution of the system. This leads to dynamics governed by diffusive transport where local changes in concentration must be balanced by material flux. We then discuss the implementation of these dynamics in Model B and Model H, which capture the essential physics of conserved phase separation with and without hydrodynamic effects. Finally, we turn to key mechanisms of phase separation such as spinodal decomposition, nucleation, and Ostwald ripening.
Most of the content presented in this chapter follows [4], [16].

2.1 Equilibrium phase separation: Free energy

We describe phase separation using a field-theoretical approach based on continuum models in terms of a scalar field $\phi(\mathbf{r}, t)$. This field can represent various physical quantities, such as a magnetization density or the concentration of two species in a binary fluid.
The first step is to define a free energy functional, a simple choice is to set

$$\mathcal{F}[\phi] = \int d\mathbf{r} \left[f(\phi) + \frac{k}{2} |\nabla \phi|^2 \right], \tag{2.1.1}$$

where the function $f(\phi)$ is the bulk free energy density:

$$f(\phi) = \frac{a}{2}\phi^2 + \frac{b}{4}\phi^4.$$

These definitions already contains some relevant physics. First the bulk free energy captures the preferred local composition of the system, the quartic function can indeed have one minima in $\phi = 0$ or, for another choice of parameters, two distinct minima, which determines the phase in the bulk of the system. Then the second term associates an energetic cost to spatial inhomogeneities.

The first step is to find the density that minimizes the bulk free energy. Consider a uniform state $\phi(\mathbf{r}) = \phi^*$, for $a > 0$ the minimum is obtained for $\phi^* = 0$, which means that the system doesn't phase separate, as it would not decrease the free energy. On the other hand $a < 0$ gives other two minima $\phi^* = \pm\phi_b = \pm\sqrt{-\frac{a}{b}}$; in this case the free energy is minimized demixing the two states. The densities $\pm\phi_b$ are called binodals.
Furthermore, on the phase diagram (fig. 2.1(b)) it is interesting to distinguish also the spinodal curve defined with the spinodal densities ϕ_s, which determines the

stability type in the phase separated regime. Between the spinodal and binodal curves, the system is metastable (small perturbations decay but large enough fluctuations can trigger phase separation), while inside the spinodal region, the system is absolutely unstable to any perturbation, no matter how small.
The spinodals are found by setting the second derivative of the bulk free energy to zero: $f''(\phi) = a + 3b\phi^2 = 0$. For $a < 0$, this gives the spinodal points $\phi_s = \pm\sqrt{-a/3b}$.

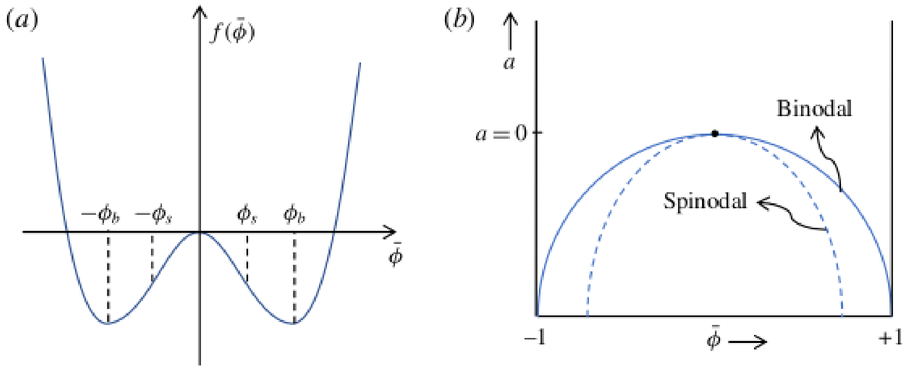

Figure 2.1: (**a**) Free energy density $f(\phi)$. (**b**) Phase diagram with spinodal and binodal curve. Under the dashed curve the system is unstable to every perturbation; between binodal and spinodal curve the system is linearly stable, but can phase-separate through other mechanisms. Figure adapted from [16].

2.2 Conserved Field

As we are interested in conserved field models, in this section we are going to describe specifically some results valid in such cases. Examples of conserved fields can be the volume fractions of different species in liquid mixtures, the composition in binary metallic alloys, or the particle concentration in colloid suspensions. The key difference from a generic field model is that the integral over all the volume of the field is constant.
Consider parameters for which the system separates in two phases, then we can use the minimization of the free energy to determine the shape of the interface at equilibrium. Since the presence of an interface is associated to an energetic cost, it will tend to minimize its area by flattening the surface.
Using the Lagrange multiplier λ to keep the total density constant we get:

$$\frac{\delta}{\delta\phi}\left[\mathcal{F} - \lambda \int d\mathbf{r}\,\phi\right] = 0.$$

But $\frac{\delta}{\delta\phi}\mathcal{F} = \mu(y)$ is the chemical potential, and subsequently $\mu = \lambda$. Call y the direction orthogonal to the interface, then $\phi(\mathbf{r}) = \phi(y)$ with boundary conditions $\phi(y) = \pm\phi_b$ for $y \to \pm\infty$.
Finally, in the bulk we find $\mu = \frac{df}{d\phi} = 0$ since $\phi = \pm\phi_b$ and it follows that $\lambda = 0$.

The differential equation we need to solve is $\mu(y) = 0$:

$$a\phi^2 + b\phi^3 - k\nabla^2\phi = 0, \tag{2.2.1}$$

which leads to

$$\phi_{eq}(y) = \pm\phi_b \tanh\left(\frac{y - y_0}{\xi_0}\right) \tag{2.2.2}$$

with y_0 the position of the interface and $\xi_0 = \sqrt{-k/2a}$ is the interface width parameter.
Looking back at eq. (2.2.1), we notice that the interface shape comes from the trade-off between the minimization of the bulk free energy, obtained with a step function on the binodals, versus a term penalizing steep gradients, with strength determined by the parameter k.
Furthermore, we define the interfacial tension at equilibrium:

$$\sigma_{eq} = \int k(\partial_y\phi_{eq}(x))^2 = \left(\frac{-8ka^3}{9b^2}\right)^{1/2}. \tag{2.2.3}$$

The surface tension represents the excess free energy per unit area due to the presence of an interface. Particles at the interface have fewer favorable interactions compared to those in the bulk phases, which implies an energetic cost.
Surface tension is responsible for several phase separation phenomena: it determines the equilibrium shape of droplets (spherical to minimize surface area), sets the energy barrier for nucleation of new phases (section 2.4.2), and provides the driving force for Ostwald ripening (section 2.4.3).

2.3 Model B and Model H

Having derived some base equilibrium properties of phase separating systems, we now turn to their dynamics, starting with the simplest case of dry systems where hydrodynamic effects are negligible. In this case, the dynamics of the conserved field ϕ is governed by the compositional current $\mathbf{J} = -M\nabla\mu$ where M is the mobility, a quantity that describes how fast the species can move through chemical potential gradients. The simplest model is:

$$\begin{cases} \dot{\phi} = -\nabla \cdot \mathbf{J} = \nabla \cdot (M\nabla\mu) \\ \mu = \frac{\delta\mathcal{F}}{\delta\phi} \end{cases}. \tag{2.3.1}$$

This set of equations is known as Model B [5] and describes phase separation dynamics in systems where particles diffuse due to chemical potential gradients, balancing the local composition with diffusive transport. The divergence of the current on the right hand side ensures the conservation of the field.
On the other hand, if particles are in a suspension, we need to take into account the effects of the fluid motion. In this case, the general equation for the dynamics of ϕ takes the form

$$\dot{\phi} + \mathbf{v} \cdot \nabla\phi = -\nabla \cdot \mathbf{J}$$

where the new left-hand side term is the advection contribution that couples the field to the fluid.
The fluid dynamics are governed by the incompressible Navier-Stokes equations:

$$\begin{cases} \rho\left(\frac{\partial \mathbf{v}}{\partial t} + \mathbf{v} \cdot \nabla\mathbf{v}\right) = \eta\nabla^2\mathbf{v} - \nabla P + \mathbf{F} \\ \nabla \cdot \mathbf{v} = 0 \end{cases} \tag{2.3.2}$$

where ρ is the fluid density, η is the viscosity, P is the pressure and $\mathbf{F}$ represents body forces acting on the fluid. In the low Reynolds number regime, typical of many phase separation processes, the inertial terms can be neglected, leading to the Stokes equations.
Finally, combining the conserved field evolution with the incompressible Navier-Stokes equations, we obtain:

$$\begin{cases} \dot{\phi} + \mathbf{v} \cdot \nabla\phi = \nabla \cdot (M\nabla\mu) \\ 0 = \eta\nabla^2\mathbf{v} - \nabla P + \mathbf{F}, \quad \nabla \cdot \mathbf{v} = 0 \quad . \\ \mu = \frac{\delta\mathcal{F}}{\delta\phi} \end{cases} \tag{2.3.3}$$

This system is known as Model H [5].
In general terms the force $\mathbf{F}$ needs to be traceless, as this contribution can be absorbed in the pressure, then a general gradient form is

$$F_i = -\nabla_j\sigma_{ij} = -k\nabla_j\left[(\nabla_i\phi)(\nabla_j\phi) - \frac{\delta_{ij}}{d}|\nabla\phi|^2\right] \tag{2.3.4}$$

where d is the system dimension.
The system up to this point is deterministic as it has no stochastic part, but in general it's interesting to include noise terms in the fluid stress $\boldsymbol{\sigma}^n$ and in the current $\mathbf{J}^n$. For example, droplets suspended in a fluid won't come into contact and coalesce unless we consider their diffusion due to noise.

Additionally, a system initialized at a density $\bar{\phi}$, between the spinodal and the binodal values, would remain uniform unless we include noise that would drive the system over the nucleation barrier.

2.4 Key mechanisms of phase separation

Phase separation dynamics are governed by distinct mechanisms that operate under different conditions and length scales. Initial state of the system relative to the spinodal and binodal curves, the presence of thermal fluctuations and hydrodynamic effects all affect differently phase separation. In this section, we examine three fundamental mechanisms: spinodal decomposition, nucleation and Ostwald ripening.

2.4.1 Spinodal decomposition

When the initial mixture state lies within the spinodal region, the system becomes linearly unstable to infinitesimal perturbations, which are amplified exponentially driving the spinodal decomposition.
The separation in domains of the two binodals is initially due to the amplification of all unstable wavelengths, the fluctuations then grow until they reach binodal values $\pm\phi_b$ and afterwards the dynamics is determined by the topology of the generated domains.

We can characterize the instability through linear analysis.
The free energy is $\mathcal{F} = \int d\mathbf{r}[a\phi^2/2 + b\phi^4/4 + k/2|\nabla\phi|^2]$, and substituting in eq. (2.3.1), we find, assuming a constant mobility

$$\dot{\phi} = M\nabla^2\mu = M\nabla^2(f'(\phi) - k\nabla^2\phi).$$

Now we linearize around a uniform density $\bar{\phi}$, this means that higher order in the gradients are neglected, and taking the Fourier transform with wavevector q, we obtain

$$\dot{\phi}_q = -Mq^2[f''(\bar{\phi}) + kq^2]\phi_q = \sigma(q)\phi_q$$

with $\sigma(q)$ the growth rate.
It's clear that for $f''(\bar{\phi}) > 0$ all the modes are stable and for $f''(\bar{\phi}) < 0$ the system is unstable with the most unstable mode $q^* = -f''(\bar{\phi})/2k$.
Finally we observe that this result is valid for Model B (eq. (2.3.1)) and also for Model H (eq. (2.3.3)), because in the latter the fluid is coupled to the density through the advection term, which does not contribute in the linear analysis.

2.4.2 Nucleation

In the metastable region (between spinodal and binodal), the system is linearly stable to small perturbations, but phase separation can still occur through nucleation of critical droplets. This process requires thermal noise to drive the system over the free energy barrier associated with creating new interfaces.
The competition between surface energy, proportional to R^2, and bulk energy gain, proportional to R^3, determines the critical radius $R_c = 2\sigma_{eq}/(f'(\phi_\varepsilon)\Delta\phi - \Delta f)$ [17], where $\Delta\phi$ and Δf are the differences between the two binodals value $\pm\phi_b$ and $\phi_\varepsilon = \phi_b + \varepsilon$ is the density of the bulk with a small supersaturatioin ε.
Droplets with radius smaller than R_c will shrink and disappear, while those larger will grow spontaneously. This mechanism is driven by thermal fluctuations and requires large deviations to nucleate a droplet.

2.4.3 Ostwald Ripening

Without noise, domain coarsening is mediated by a diffusion mechanism due to $M\nabla^2\mu$ which depends on the interface curvature, this process is called Ostwald ripening.
Consider a spherical droplet of radius R with interfacial tension σ_{eq}. At equilibrium, the surface tension is balanced by a pressure difference called Laplace pressure. By considering force balance on a hemispherical droplet, where the surface tension force $2\pi R\sigma_{eq}$ acting on the perimeter balances the pressure net force $\pi R^2\Delta P$ on the interface, we find the Laplace pressure:

$$2\pi R\sigma_{eq} = \pi R^2 \Delta P \quad \Rightarrow \quad \Delta P = \frac{2\sigma_{eq}}{R}.$$

The Laplace pressure is given by the osmotic pressure $\Delta P = \Delta[\phi\mu(\phi) - f(\phi)]$, then the bulk densities are $\phi_{A,B} = \pm\phi_b + \delta$, with the binodals shifted by $\delta = \frac{\sigma_{eq}}{-2a\phi_b R}$.
Since δ is inversely proportional to R, smaller droplets have higher chemical potential, while larger droplets have lower one. This creates a chemical potential gradient from small to large droplets.

Consider a small ambient supersaturation $\varepsilon < \delta$, such that far from the droplet $\phi(r \to \infty) = -\phi_b + \varepsilon$. Under quasi-static conditions ($\dot{\phi} = -\nabla \cdot \mathbf{J} = 0$), we solve for the spherically symmetric concentration profile $\phi(r) = -\phi_b + \tilde{\phi}(r)$ with boundary conditions $\tilde{\phi}(\infty) = \varepsilon$ and $\tilde{\phi}(R) = \delta$. For small supersaturation, the chemical potential is $\mu = -2a\tilde{\phi}$ and the diffusion equation becomes $\nabla^2\tilde{\phi} = 0$, with solution $\tilde{\phi}(r) = \varepsilon + (\delta - \varepsilon)R/r$.
The radial flux just outside the droplet then becomes

$$J = -2aM\partial_r\tilde{\phi}|_{r=R} = 2aM(\delta - \varepsilon)\frac{1}{R},$$

conservation of mass at the interface requires that the flux through the surface equals the rate of volume change times the concentration jump:

$$J 4\pi R^2 = 2\phi_b \frac{d}{dt}\left(\frac{4\pi R^3}{3}\right),$$

from which we get

$$\dot{R} = -\frac{aM}{\phi_b R}\left(\varepsilon + \frac{\sigma_{eq}}{2a\phi_b R}\right) = \frac{\sigma_{eq} M}{2\phi_b^2}\frac{1}{R}\left(\frac{1}{R^*} - \frac{1}{R}\right).$$

The critical radius that gives $\dot{R} = 0$ is $R^* = \frac{\sigma_{eq}}{-2a\varepsilon\phi_b}$. Droplets with $R < R^*$ shrink and eventually disappear, while those with $R > R^*$ grow at the expense of smaller ones.
Finally one finds the time scaling of typical radius $R(t) \sim t^{1/3}$.

2.4.4 Coarsening in the Hydrodynamic Scaling Regime

When fluid flow is included, as in Model H, coarsening pathways mediated by the flow emerge, which determine a richer phenomenology than the one captured by the dry case (Model B). It is important to note that the modification of coarsening in Model H due to hydrodynamics takes place only when the system is bicontinuous, which means that both phases form interconnected domains and typically occurs when the volume fractions of the two phases are comparable.
To characterize the different regimes and their scaling laws, we define the characteristic domain size $L(t)$ and study which terms dominate in the Navier-Stokes equation eq. (2.3.2). Using dimensional arguments, we can estimate the scaling of each term by recognizing that velocities scale as $\mathbf{v} \sim \dot{L}$ and spatial derivatives as $\nabla \sim L^{-1}$.
This gives us the following scalings: the thermodynamic stress $\mathbf{F} \sim \sigma_{eq} L^{-2}$, the inertial terms $\rho\partial_t \mathbf{v} \sim \rho\ddot{L}$ and $\rho(\mathbf{v}\cdot\nabla)\mathbf{v} \sim \rho(\dot{L})^2 L^{-1}$, and the viscous contribution $\eta\nabla^2\mathbf{v} \sim \eta\dot{L}L^{-2}$. Moreover, dry diffusion scales as $M\nabla^2\mu \sim M\sigma_{eq}L^{-3}$ and the advection term as $(\mathbf{v}\cdot\nabla)\phi \sim \sigma_{eq}L^{-1}\eta^{-1}$.
The regime transitions occur when different terms in the equations become comparable. By comparing the magnitudes of these terms, we get the crossover length scales and the power-law behaviors.
First we note that advective transport, that is the fluid contribution, dominates over the diffusion at $L \gg (M\eta)^{1/2}$. In this hydrodynamic regime, we can distinguish two sub-regimes based on the Reynolds number. At low Reynolds number, we obtain the Viscous Hydrodynamic regime by neglecting inertial terms and balancing the thermodynamic stress with the viscous contribution: $\eta\nabla^2\mathbf{v} \sim \mathbf{F}$. This gives

$\eta \dot{L} L^{-2} \sim \sigma_{eq} L^{-2}$, yielding

$$\dot{L} \sim \frac{\sigma_{eq}}{\eta} \quad \Rightarrow \quad L(t) \sim \frac{\sigma_{eq}}{\eta} t,$$

which is valid for $L \ll \eta^2/(\sigma_{eq}\rho)$.

At later times, when inertial terms become dominant over viscous ones, we enter the Inertial Hydrodynamic regime. Here we balance inertia with the thermodynamic stress: $\rho(\partial_t \mathbf{v} + (\mathbf{v} \cdot \nabla)\mathbf{v}) \sim \mathbf{F}$, which gives $\rho(\dot{L} L^{-1} + \dot{L}^2 L^{-1}) \sim \sigma_{eq} L^{-2}$ and $L(t) \sim \left(\frac{\sigma_{eq}}{\rho}\right)^{1/3} t^{2/3}$.

In summary, there are three principal growth regimes for phase separation, whose scalings are reported in the following table.

Mechanism	**Scaling**	**Length-scale**
Diffusive Coarsening	$L \sim t^{1/3}$	$L \ll (M\eta)^{1/2}$
Viscous Hydrodynamic	$L \sim t$	$(M\eta)^{1/2} \ll L \ll \eta^2/\sigma_{eq}\rho$
Inertial Hydrodynamic	$L \sim t^{2/3}$	$\eta^2/\sigma_{eq}\rho \ll L$

Table 2.1: Summary of coarsening regimes in passive phase separation.

3. Active Phase Separation

The paradigm shift introduced by activity is fundamental. In passive systems, the system attains the minimum of the free energy in the statistically steady state. Active systems by contrast lack an equilibrium state. Detailed balance is violated through constant injection of energy at the particle level, where individual components use this surplus to produce work. This can cause the emergence of phase separation even in contexts where it is impossible at equilibrium, as if particles purely repel each other.

The field-theoretical approach captures universal features across diverse systems. Extending the framework developed for equilibrium phase separation, continuum models that incorporate activity through additional terms that break detailed balance have been constructed in the literature [3]. This approach is quite general: by identifying the relevant symmetries and conservation laws, we can write down effective equations that capture the essential physics without the need for a detailed knowledge of microscopic interactions.

We employ such continuum framework to describe active systems, considering a single conserved order parameter $\phi(\mathbf{r}, t)$ that can be interpreted as the coarse-grained particle density. The continuum description emerges through the coarse-graining of microscopic systems. If ϕ is the only slow variable at large scales, this approach can give a generic description of phase separation, independent of the microscopic details of the system. This separation of scales is what makes the field-theoretical approach so powerful: it allows us to make quantitative predictions about macroscopic behavior without solving the full many-body problem at the microscopic level.

The active counterparts of the models discussed before are Active Model B+ [7] and Active Model H [1]. The first corresponds to the dry limit and the activity is introduced in the compositional current J as there is no fluid coupling. In Active Model B+ the binodal values are modified and the Ostwald process can be reversed. Active Model H on the other hand corresponds to the fully wet case, in this case activity modifies the coarsening dynamics, leading to an arrest of domain growth in contractile systems.

3.1 Active Model H

In this section we extend Model H (section 2.3) to an active model by introducing an active term in the stress tensor. The governing equations read

$$\begin{cases} \dot{\phi} + \mathbf{v} \cdot \nabla \phi = \nabla (M \nabla \mu) \\ 0 = \eta \nabla^2 \mathbf{v} - \nabla P + \mathbf{F}^p + \mathbf{F}^a, \quad \nabla \cdot \mathbf{v} = 0 \\ \mu = \frac{\delta \mathcal{F}}{\delta \phi} \end{cases} , \tag{3.1.1}$$

where we distinguish the active stress $\mathbf{F}^a$ from the passive stress $\mathbf{F}^p$ which coincides with the one from eq. (2.3.3). For the specific form of the active stress, we

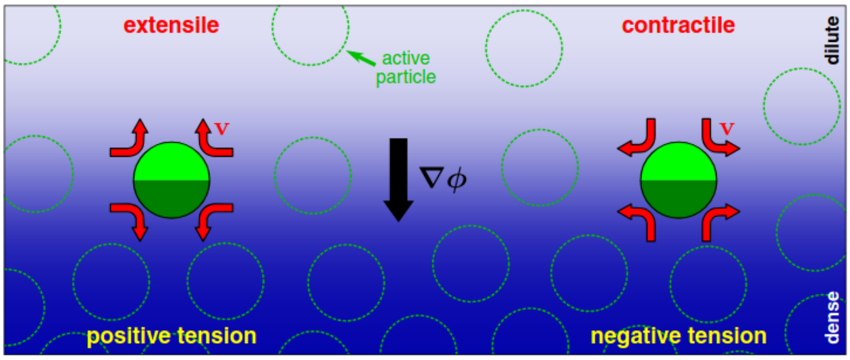

Figure 3.1: Schematic view of extensile and contractile fluid flow around active swimmers aligned with the normal of the interface ($\nabla\phi$), between a dense and a dilute domains. Figure adapted from [1].

take the lowest order second rank deviatoric tensor constructable from ϕ and its gradients, which has the same functional form as the passive stress eq. (2.3.4) but with a different prefactor:

$$F_i^a = -(\tilde{k}-k)\nabla_j\sigma_{ij} = -(\tilde{k}-k)\nabla_j\left[(\nabla_i\phi)(\nabla_j\phi) - \frac{\delta_{ij}}{d}|\nabla\phi|^2\right],$$

where k is the same parameter appearing in the free energy eq. (2.1.1), $\tilde{k}$ is an independent active parameter and d is the dimension of the system. The total stress becomes

$$\mathbf{F} = \mathbf{F}^p + \mathbf{F}^a = -\tilde{k}\nabla\cdot\boldsymbol{\sigma}.$$

Although the functional form is identical to the equilibrium case, the mismatch between k and $\tilde{k}$ breaks detailed balance, making a free energy description impossible.

The sign of the active prefactor $(\tilde{k}-k)$ classifies the system: positive values correspond to extensile systems, while negative values correspond to contractile ones. This classification originates from how self-propelled swimmers drive fluid flow primarily through a force dipole along their axis. Contractile particles (e.g. algae) generate outward forces that draw fluid from the poles and expel it radially, while extensile particles (e.g. swimming bacteria) do the opposite [6]. The microscopic view of swimmer forces can be linked to the continuum description of Active Model H, giving $(\tilde{k}-k) > 0$ extensile swimmers and $(\tilde{k}-k) < 0$ contractile ones [1].

3.1.1 Surface Tensions and Ostwald Ripening

Activity modifies the interfacial physics by generating a second surface tension, which doesn't affect Ostwald ripening, but induces a new type of instability. Its

value is $\sigma_M = \sigma_{eq}\tilde{k}/k$ at the interfaces where swimmers point along the surface normal, that is along the order parameter gradient [18].
Contractile swimmers expel fluid in the interfacial plane, causing stretching, whereas extensile swimmers do the opposite. This creates the resulting tension σ_M, which is negative for contractile swimmers and positive for extensile ones.
In the extensile case with positive tension $\sigma_M > 0$, the dynamics follow conventional Ostwald ripening as described in section 2.4. On the other hand, contractile systems ($\sigma_M < 0$) causes large droplets to split (self-shearing) due to the negative surface tension. In the latter case, the phenomenon is balanced by the Ostwald ripening: small droplets evaporate, while large ones grow until they in turn become unstable. This creates a dynamical steady-state where droplets splitting is followed by the diffusive growth or disappearance of the offspring.
This behavior has been observed in Active Model H, leading to microphase separation; later in section 4.4 it will be interpreted as an instability of capillary waves.

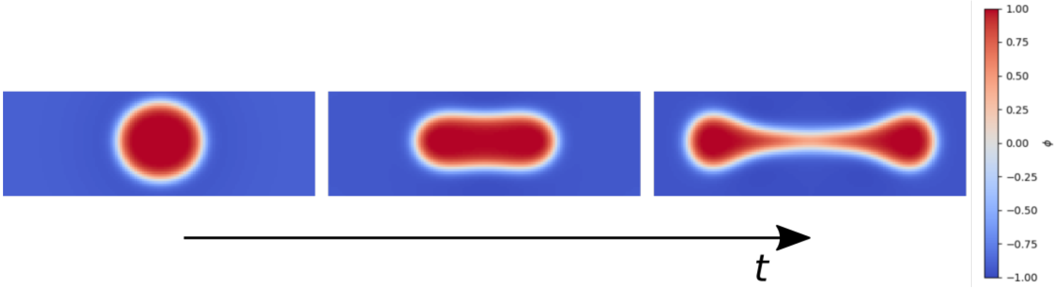

Figure 3.2: Visualization of a droplet self-shearing instability for a contractile system.

Next we describe how activity affects the coarsening dynamics, including hydrodynamical effects. We analyze the evolution of the characteristic domain size $L(t)$ following [1].
In the viscous regime, ignoring inertia terms, by a power counting argument we find

$$\dot{L} \approx \alpha \frac{\sigma_{eq}}{L^2} + \beta \frac{\sigma_M}{\eta}$$

with α and β dimensionless constants.
The first term represent the standard diffusive contribution, where the chemical potential gradient scales as $\nabla\mu \sim \sigma_{eq}/L^2$, leading to the passive growth $L \sim t^{1/3}$. The second contains the active contribution, it originates balancing the viscous terms $\eta\nabla^2\mathbf{v} \sim \eta\dot{L}L^{-2}$ with the active stress $\mathbf{F} \sim \sigma_M L^{-2}$. This term is independent of L and contributes with a constant driving force to the coarsening of system domains.
For extensive systems $\sigma_M > 0$, we obtain the diffusive ($L \sim t^{1/3}$) and viscous hydrodynamic ($L \sim t$) regimes as in the passive case section 2.4.
But for contractile swimmers, when the activity is strong enough we can have a dynamical arrest $\dot{L} = 0$ at the scale $L^* \sim (\eta\sigma_{eq}/|\sigma_M|)^{1/2}$, where the diffusive coarsening is opposed by activity.

4. Active Model H with Friction

4.1 Motivation

Active Model H offers key insights into active phase separation, predicting a rich range of phenomena that significantly affect coarsening dynamics compared to passive systems. However, in its standard formulation, it assumes purely wet dynamics where momentum is exactly conserved throughout the system. This assumption is not realistic for most experimental realizations of active systems.
Active particles often move in fluid environments but do so in close proximity to boundaries or substrates with which they exchange momentum. Most experimentally studied active systems operate in quasi-two-dimensional geometries under screened fluid flow conditions. For example cell colonies growing on surfaces [13], swimming bacteria interacting with microstructures [19] and confined microtubule bundles [14]. In these systems, the substrate or confining walls provide a momentum sink, effectively introducing friction in the dynamics.
The introduction of friction modifies the nature of hydrodynamic interactions in non-trivial ways. One might initially expect that increasing friction would simply reduce the system to the dry case, analogous to active variations of Model B [7], where hydrodynamic effects are entirely absent. However, it remains unclear whether this dry limit is actually recovered at large scales, as fluid-mediated interactions can still generate long-range forces even under screening [2], [20].
The study of friction is then interesting both from an experimental perspective, giving a theoretical background on the phenomenology of many real systems; and from a theoretical point of view as the friction parameter connects between two fundamentally different regimes of active matter dynamics.

Below, we investigate how friction modifies active phase separation by extending the Active Model H as in [2].
Through linear stability analysis, we examine how friction affects the stability of interfaces and the emergence of capillary wave instabilities that can lead to microphase separation. Even including friction, interfaces can become unstable, when the activity surpass a certain threshold; as a byproduct, we further shows that the shape instability governing Active Model H is induced by capillary wave instability. Finally, we present numerical simulations that map out the phase diagram, revealing how friction alters the phase separation behavior and that support the analytical results.

4.2 Model and interface description

The equations of the model are identical to the ones of Active Model H eq. (3.1.1) with the addition of a friction term in the Navier-Stokes equation:

$$\begin{cases} \partial_t\phi + \mathbf{v}\cdot\nabla\phi = M\nabla^2\mu, \\ 0 = -\Gamma\mathbf{v} + \eta\nabla^2\mathbf{v} + \nabla P + \mathbf{F}, \quad \nabla\cdot\mathbf{v} \quad , \\ \mu = \frac{\delta\mathcal{F}}{\delta\phi} \end{cases} \tag{4.2.1}$$

with a constant mobility M and the usual ϕ^4 free energy $\mathcal{F} = \int d\mathbf{r}[f(\phi) + k/2|\nabla\phi|^2]$ with bulk free energy density $f(\phi) = a/2\,\phi^2 + b/4\,\phi^4$.
In the flow equation Γ is frictional dampening of the flow and, since the momentum is not conserved due to friction, the active stress cannot be written as the divergence of a local stress tensor, then including higher orders up to $\mathcal{O}(\nabla^3\phi^3)$ we have

$$F_i = -\nabla_j\sigma_{ij} + K_1\phi\nabla_i\phi(\nabla^2\phi) + K_2|\nabla\phi|^2\nabla_i\phi$$

with the usual $\sigma_{ij} = \tilde{k}\left[(\nabla_i\phi)(\nabla_j\phi) - \delta_{ij}/d|\nabla\phi|^2\right]$.

4.3 Binodals and Ostwald ripening

In this section, we address two important aspects of phase separation dynamics in Active Model H with friction: the determination of binodal curves and the coarsening process through Ostwald ripening.
Both phenomena reduce to their passive Model B (section 2.3) due to the suppression of fluid motion, ignoring effects given by the interface curvature.

4.3.1 Binodal Analysis

To determine the binodal curves, we consider a flat interface between two coexisting phases with normal along y and $\mathbf{x}$ the directions parallel to it, then the interface profile is defined with $h(\mathbf{x},t)$.
By symmetry the field $\phi(\mathbf{r},t)$ should depend only on the direction normal to the interface, then we have the ansatz on the density profile:

$$\phi(y,\mathbf{x},t) = \varphi(y - h(\mathbf{x},t)), \tag{4.3.1}$$

where $\varphi(y - h(\mathbf{x},t)) = \phi_{eq}(y)$ is the equilibrium interface profile eq. (2.2.2).
The boundary conditions for $\phi(\mathbf{r}) = \varphi(y)$ are $\varphi \to \varphi_\pm$ as $y \to \pm\infty$ and for the velocity field, $\mathbf{v} = 0$ at infinity.
Given the translational invariance parallel to the interface, the velocity field can only depend on the normal direction, $\mathbf{v}(\mathbf{r}) = \mathbf{v}(y)$ and parallel components are null by symmetry. Then the incompressibility equation $\nabla\cdot\mathbf{v} = \partial_y v_y = 0$ with the

boundary conditions lead to $v_y = 0$ and

$$\mathbf{v} = 0.$$

Active Model H equations reduce to the passive Model B dynamics: $\dot{\phi} = M\nabla^2\mu$ for which the binodals are $\varphi_\pm = \pm\phi_b = \pm\sqrt{-a/b}$.

4.3.2 Ostwald Ripening Analysis

For Ostwald ripening, we consider the evolution of a spherical droplet of radius $R(t)$ in a supersaturated medium. The relevant direction is the radial one and the interface profile is $R(t)$, then ignoring correction due to the curvature we have

$$\phi(\mathbf{r}, t) = \varphi(r - R(t)). \tag{4.3.2}$$

We focus now on the Navier-Stokes equation with friction and rewrite the fluid stress in this simplified setting:

$$\begin{aligned}
F_r &= -\tilde{k}\,\frac{1}{r^2}\partial_r\left(r^2\frac{d-1}{d}(\partial_r\varphi)^2\right) + K_1\varphi(\partial_r\varphi)(\partial_r^2\varphi) + K_2(\partial_r\varphi)^3 = \\
&= -\tilde{k}\,\frac{d-1}{d}\partial_r\left((\partial_r\varphi)^2 - \int^r dr'(-2)\frac{1}{r'^3}r'^2(\partial_{r'}\varphi)^2\right) + \\
&\qquad + K_1\partial_r\left[\frac{1}{2}\varphi(\partial_r\varphi)^2 - \frac{1}{2}\int^r dr'(\partial_{r'}\varphi)^3\right] + K_2\partial_r\left[\int^r dr'(\partial_{r'}\varphi)^3\right] = \\
&= \partial_r\left\{\tilde{k}\,\frac{d-1}{d}\left[-(\partial_r\varphi)^2 + 2\int^r dr'\frac{(\partial_{r'}\varphi)^2}{r'}\right] + \frac{K_1}{2}\varphi(\partial_r\varphi)^2 + \left(K_2 - \frac{K_1}{2}\right)\int^r dr'(\partial_{r'}\varphi)^3\right\}.
\end{aligned}$$

The stress can be written as a full derivative, but this means that it can be absorbed in the pressure contribution $\mathbf{F} - \nabla P = -\nabla\tilde{P}$. The Navier-Stokes equation then becomes

$$\Gamma\mathbf{v} = \eta\nabla^2\mathbf{v} - \nabla\tilde{P}. \tag{4.3.3}$$

On the other hands $\mathbf{v}$ satisfies the incompressibility condition in spherical coordinates:

$$\nabla\cdot\mathbf{v} = \frac{1}{r^2}\frac{\partial}{\partial r}(r^2 v_r) = 0. \tag{4.3.4}$$

This implies $r^2 v_r = [\text{const.}]$ and $\mathbf{v} = 0$.
Moreover, this implies that also the pressure gradient vanish and Active Model H

with friction again reduces to passive Model B dynamics.
Droplet dynamics then follows the classical Ostwald ripening, where droplets under a critical radius vanish and above grows indefinitely.

4.4 Capillary Waves

We now examine the linear stability of interfaces by analyzing the dynamics of capillary waves, small perturbations that propagate along the interface between coexisting phases.
First we observe that the NSE with friction can be solved (appendix A) and, using an implicit sum notation, the velocity field takes the form

$$v_i(\mathbf{r}) = \int d\mathbf{r}' \, G_{ij}(\mathbf{r}-\mathbf{r}')F_j(\mathbf{r}') \tag{4.4.1}$$

where G_{ij} is the modified Oseen tensor whose Fourier transform is

$$\frac{\hat{G}_{ij}}{8\pi\eta} = \frac{\delta_{ij}}{\eta q^2+\Gamma} - \frac{q_i q_j}{q^2(\eta q^2+\Gamma)}.$$

Then the model equations becomes

$$\begin{cases} \partial_t\phi + \nabla_i\phi \int d\mathbf{r}' G_{ij}(\mathbf{r}-\mathbf{r}')F_j(\mathbf{r}') = M\nabla^2\mu \\ \mu = \frac{\delta}{\delta\phi}\int d\mathbf{r}\left[f(\phi)+\frac{k}{2}|\nabla\phi|^2\right] = f'(\phi) - k\nabla^2\phi \end{cases} . \tag{4.4.2}$$

First we substitute the ansatz for a flat interface eq. (4.3.1) and setting $u = y - h(\mathbf{x},t)$ we get

$$\varphi'(u)\partial_t h + \nabla_i\varphi(u) \int d\mathbf{r}' G_{ij}(\mathbf{r}-\mathbf{r}')F_j(\mathbf{r}') = M\nabla^2\mu. \tag{4.4.3}$$

The next step is to approximate to the linear order the equation, the only term that leads to non-linearities is the advection term. In appendix B we carried on this calculation, obtaining

$$\partial_t h_q = -\sigma_{\mathrm{eq}} q^2 \left[\frac{\tilde{k}}{k}\mathcal{T}_{yy}(q,0) + \frac{2Mq}{A_{\mathrm{eq}}(q)}\right] h_q, \tag{4.4.4}$$

where we defined $A_{\text{eq}}(q) = \int dy_1\, dy_2\, e^{-q|y_1-y_2|}\varphi'(u_1)\varphi'(u_2)$ and the function $\mathcal{T}_{yy}(q,0)$ is the transformed Oseen tensor obtained in appendix A:

$$\mathcal{T}_{yy}(q,0) = \frac{1}{2\Gamma}\left(q - \frac{q^2}{\sqrt{\lambda^2+q^2}}\right).$$

with $\lambda^2 = \Gamma/\eta$.
And in the limit of small q we get

$$\partial_t h_q = -\frac{\sigma_{\text{eq}}M}{2}\left[\frac{\tilde{k}}{k\Gamma M}\left(1 - \frac{q}{\sqrt{\lambda^2+q^2}}\right) + \frac{1}{(\phi_b)^2}\right] q^3 h_q, \tag{4.4.5}$$

If $\Gamma \gg q$, the system exhibits a cubic dispersion relation:

$$\partial_t h_q = -\frac{\sigma_{\text{eq}}M}{2}\left(\frac{1}{\Gamma M}\frac{\tilde{k}}{k} + \frac{1}{(\phi_b)^2}\right) q^3 h_q. \tag{4.4.6}$$

The q^3 scaling corresponds to the one found in Active Model B [8], but lacks a linear term in q found in Active Model H [21]. Interestingly, an instability emerges by the interplay of the activity strength with the friction. The system needs to show a strong contractile behavior, below a certain threshold set by the friction in order to observe an instability of arbitrarily small modes, which is

$$\tilde{k}^* = -\frac{\Gamma M k}{(\phi_b)^2}. \tag{4.4.7}$$

On the other hand, in the limit of vanishing friction with $\Gamma \ll q$, the Oseen tensor becomes

$$\mathcal{T}_{yy}(q) = \frac{1}{2\Gamma}\left(q - \frac{q}{\sqrt{1+(\lambda/q)^2}}\right) = \frac{1}{2\Gamma}\left(q - q + \frac{1}{2}\frac{\lambda^2}{q}\right) = \frac{1}{4\eta}\frac{1}{q},$$

which leads to

$$\partial_t h_q = -\sigma_{\text{eq}}M\left(\frac{1}{4\eta M q}\frac{\tilde{k}}{k} + \frac{2Mq}{(2\phi_b)^2}\right) q^2 h_q \sim -\frac{\sigma_{\text{eq}}\tilde{k}}{4\eta k} q h_q. \tag{4.4.8}$$

In this regime, the dynamics is dominated by the q term which corresponds to the ordinary Active Model H [21] and this demonstrates that the interfacial instabilities in Active Model H are fundamentally driven by capillary wave dynamics.

Finally, we can analyze the growth rate $g(q)$, defined with

$$g(q) = -\frac{\sigma_{\text{eq}} M}{2}\left[\frac{\tilde{k}}{k\Gamma M}\left(1 - \frac{q}{\sqrt{\lambda^2 + q^2}}\right) + \frac{1}{(\phi_b)^2}\right] q^3. \tag{4.4.9}$$

In particular, the dimensionless factor in the brackets

$$\mathcal{G}(\Gamma M, q) = \frac{\tilde{k}}{k\Gamma M}\left(1 - \frac{q}{\sqrt{\lambda^2 + q^2}}\right) + \frac{1}{(\phi_b)^2} \tag{4.4.10}$$

determines the universal shape of the growth rate curve as a function of the parameters.
For $\tilde{k} < \tilde{k}^*$, the system exhibits a band of unstable modes with a maximum growth rate associated to the most unstable mode q_{max}, which determines the characteristic wavelength of the instability.
Finally, the dependence of both the most unstable mode and its associated growth rate on the friction parameter is shown in fig. 4.2. As Γ increases q_{max} decreases, until it reaches zero when $\tilde{k} = \tilde{k}^*$ and the growth rate tends to zero.

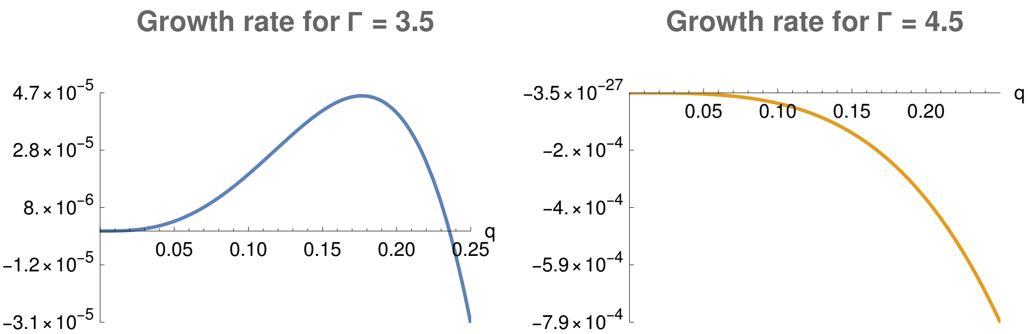
Growth rate for Γ = 3.5

Growth rate for Γ = 4.5

Figure 4.1: Growth rate defined with eq. (4.4.9), with $\Gamma = 3.5$ (left plot) and $\Gamma = 4.5$ (right plot). For both we set $\tilde{k} = -4$, $k = 1$, $M = 1$, $\eta = 1$ and $\phi_b = 1$.

4.5 Numerical Methods

The numerical solution of Active Model H equations presents significant computational challenges due to their nonlinear and multi-scale nature. The system couples

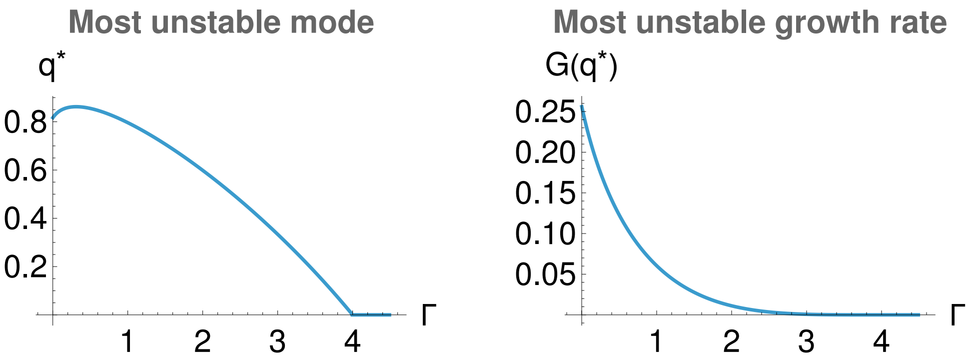

Figure 4.2: The left image is the wavevector that maximizes the growth rate eq. (4.4.9) at each value of Γ and the right image is the corresponding maximum growth rate. We set $\tilde{k} = -4$, $k = 1$, $M = 1$, $\eta = 1$ and $\phi_b = 1$.

the order parameter ϕ with the Navier-Stokes equation for the velocity field $\mathbf{v}$, both containing nonlinear terms. To solve numerically the system, we have adapted and extended the cuPSS library developed in [22], which provides a robust framework for pseudo-spectral integration of stochastic partial differential equations on GPUs.

Traditional spectral methods offers the advantage of high numerical stability with respect to space discretization, especially when the equations include many gradient terms. But they become insufficient when dealing with nonlinear terms, sinces in Fourier space they are represented by convolutions.
Pseudo-spectral methods overcome this limitation by treating differently non-linear or mixed terms, derivatives are computed in Fourier space where they reduce to simple multiplications, while nonlinear terms are evaluated in real space where the computation is easier. This offers a speedup since transforming to and from Fourier space has a cost $\mathcal{O}(N \log N)$ while the convolution of real field polynomial of order n takes $\mathcal{O}(N^2)$, where N is the real space discretization.
When dealing with discrete spectral methods, a critical issue is aliasing. To understand this problem, consider the field $\phi(x)$ and the discretization of a one-dimensional space of size N, in points distant Δx. Then in Fourier space the frequencies have separation $\Delta q = 2\pi/(N\Delta x)$ and we can take $q_i \in (-\pi/\Delta x, \pi/\Delta x)$. The fourier tranform of the field is $\phi(x) = \sum_{q_j} \hat{\phi}(q_j) \exp(iq_j x)$ and a quadratic nonlinearity becomes

$$\phi(x)^2 = \sum_{q_j, q_l} \hat{\phi}(q_j)\hat{\phi}(q_l) \exp(i(q_j + q_l)x).$$

Clearly some frequencies leads to $q_j + q_l > \pi/\Delta x$, which gives a contribution to a lower mode $q_j + q_l - 2\pi$, because of the periodic nature of Fourier frequencies.
The solution adopted in this library is to set to zero the amplitudes that create alias-

ing artifacts and use them to compute non-linearities. Specifically if a field has a non-linearity of order n then the wavevenumbers q such that $nq > 2\pi/\Delta x - q$ or $nq < -2\pi/\Delta x + q$ are set to zero, combining the two we have $|q| > 2\pi/[(n+1)\Delta x]$, which gives the de-aliasing rule for a generic polynomial non-linearity.
Finally, as we split linear from non-linear terms, we employ respectively different integration schemes. First we note that the library includes the possibility of applying some noise to the system and to integrate it we need to choose a time discretization. What the code does is to implement a fully implicit method, the Milstein scheme, for the linear terms, which gives significant numerical stability; and the Euler-Maruyama step for the mixed or non-linear terms, which sacrifies some numerical stability in favor of higher speed.
Moreover it is worth to mention that this code can run on GPU, achieving better performances than CPU-based libraries, and enabling exploration of larger systems and more parameter regimes.

4.6 Numerical Results

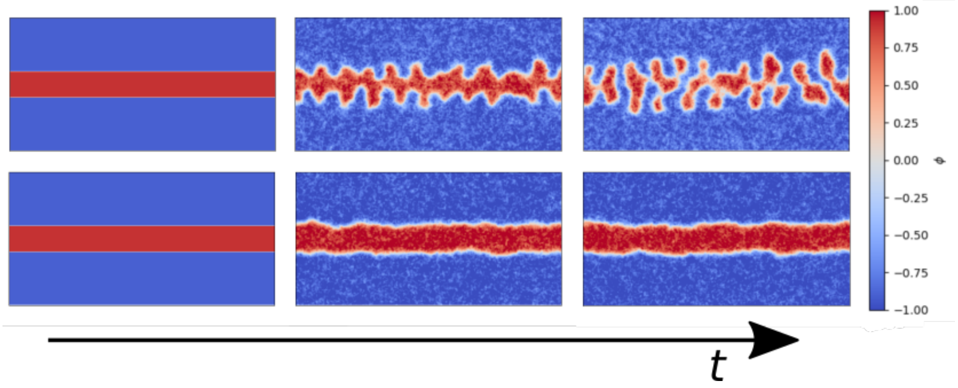

Figure 4.3: Interface stability simulations. Snapshots are taken at $t = 0$, $t = 2.5 \cdot 10^5$ and $t = 5 \cdot 10^4$. Simulation above has $\Gamma = 1$, $k = 1$, $M = 1$, $\phi_b = 1$ and $\tilde{k} = -4$. Simulation below has the same parameters but $\tilde{k} = -0.4$.

In this section we report our numerical results to provide some validation of the theoretical predictions of section 4.4. In particular we will address two key aspects of capillary waves: verification of the critical activity threshold and study the behavior at constant ΓM.

In order to observe the capillary wave instability, the system was initialized as a flat band of the density at the binodal ϕ_b, in a domain of the other binodal $-\phi_b$ (left frames of fig. 4.3). To perturb the interface, the field is evolved with zero-average and unit variance gaussian noise η_t that in the model would take the form of a small stochastic current $\mathbf{J}^n = 2D\eta_t$, and the fluid with a zero-average stochastic force $\mathbf{F}^n$ which we assume that satisfies the fluctuation-dissipation theorem:

$$\langle \hat{F}_i^n(\mathbf{p},\omega)\hat{F}_j^n(\mathbf{p}',\omega')\rangle = (2\pi^{d+2})2D(\Gamma + \eta|\mathbf{p}|^2)\delta_{ij}\delta(\mathbf{p}+\mathbf{p}')\delta(\omega+\omega')$$

written in fourier space with wavevector $\mathbf{p} = (\mathbf{q}, q_y)$.
Then the model reads

$$\begin{cases} \partial_t \phi + \mathbf{v} \cdot \nabla \phi = -\nabla \cdot (\mathbf{J} + \mathbf{J}^n) \\ 0 = -\Gamma \mathbf{v} + \eta \nabla^2 \mathbf{v} - \nabla P - \mathbf{F} + \mathbf{F}^{\mathbf{n}} \end{cases} . \tag{4.6.1}$$

It is interesting to note that considering only a stochastic current in the field equation, that is evolving the system with effectively two temperature: positive temperature and non-zero noise for the field, zero temperature and no noise for the fluid, introduced some artifacts in the system. Although the results were qualitatively similar, we found that the binodals were modified at low mobility $M \approx 0.1$. This is an important observation as current studies of Active Model H introduce noise exclusively on the field, possibly probing a different phenomenology from the one temperature model.

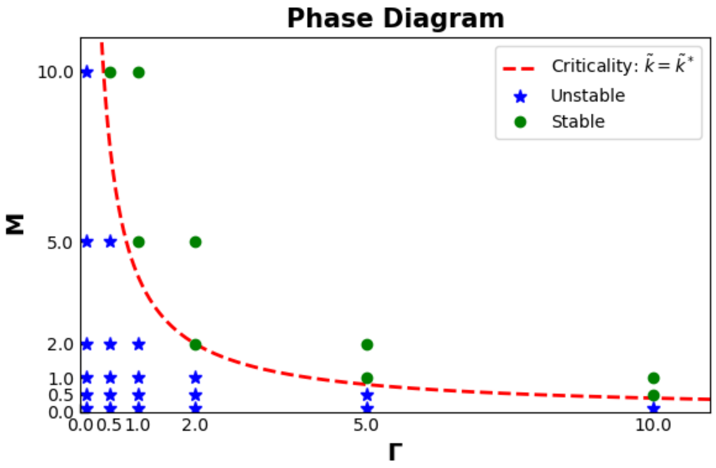

Figure 4.4: Active Model H with friction phase diagram. The dashed line represent the critical curve that separates the unstable region (below) from the stable one (above).

The predicted critical activity is $\tilde{k}^* = -\Gamma M k/(\phi_b)^2$, we verified it varying both Γ and $\tilde{k}$, spanning the two regions in fig. 4.4. The simulations are in very good agreement with the result for a wide range of parameters (fig. 4.4,fig. C.1), although we noted that the binodals were modified at low mobility $M \sim 0.1$; a phenomenon we are still investigating.
Next we observe that substituting $q = y\sqrt{\Gamma/\eta}$ in eq. (4.4.9), we find

$$g(y) = -\frac{\sigma_{eq} M}{2} \left(\frac{\Gamma}{\eta}\right)^{3/2} \left[\frac{\tilde{k}}{k\Gamma M}\left(1 - \frac{y}{\sqrt{1+y^2}}\right) + \frac{1}{(\phi_b)^2}\right] y^3. \tag{4.6.2}$$

This means that the maximum at y_{max} does not change if we keep the quantity

$\tilde{k}\phi_b^2/k\Gamma M$ constant. We can check this prediction by varying the friction and the mobility such that $\Gamma M = [\text{const.}]$ and computing $q_{max}/\sqrt{\Gamma}$. To find the most unstable frequency q_{max}, predicted in eq. (4.6.2), we tracked the interface and, after transforming to the Fourier space, we computed the dominant wavevector q at early times, when curvature effects are negligible. The values of $q_{max}/\sqrt{\Gamma}$ (shown in fig. 4.5) differ slightly; however, this deviation is not surprising given the several orders of magnitude spanned by Γ. Similarly, our attempts to retrieve the most unstable mode from fig. 4.2 were unsuccessful despite the agreement found for the phase diagram. We hypothesize then that the linear analysis correctly capture the onset of instabilities, but perturbations are significativly affected by other mechanisms perhaps described at a non-linear level.

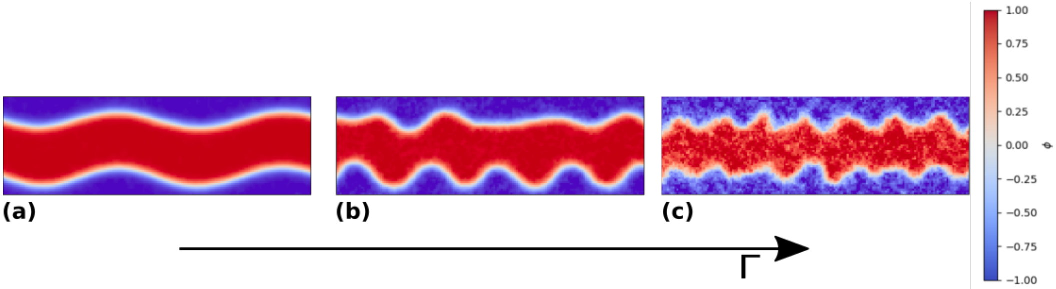

Figure 4.5: Detail of capillary instability simulations keeping $\Gamma M = [\text{const.}]$. For all the simulations we set $\tilde{k} = -4$, $k = 1$, $\phi_b = 1$, $D = 0.05$ and system size $L_x = 256$, $L_y = 128$.
(a): $\Gamma = 10^{-2}$, $M = 10^2$, $q_{max} \approx 0.07$ and $q_{max}/\sqrt{\Gamma} \approx 0.7$.
(b): $\Gamma = 10^{-1}$, $M = 10$, $q_{max} \approx 0.2$ and $q_{max}/\sqrt{\Gamma} \approx 0.6$.
(c): $\Gamma = 1$, $M = 1$, $q_{max} \approx 0.3$ and $q_{max}/\sqrt{\Gamma} \approx 0.3$.

5. Conclusions

This thesis investigates the role of friction in active phase separation by extending Active Model H to include momentum dissipation through substrate interactions, studying fluid flows in a more realistic setup. This extension addresses a critical gap between theoretical models and experimental realizations. The former are idealized models where, either the fluid is not considered at all (Model B) or they assume exact conservation of fluid momentum (Model H); however real systems operate in quasi-two-dimensional geometries where the fluid exchanges momentum with boundaries.

First we found that in the extension of Active Model H, binodals and the Ostwald process are reduced to the ones of Model B, because the incompressibility constraint effectively removes the fluid contribution.

Moreover, our findings establish that interface stability in contractile active systems is governed by a critical activity threshold given by eq. (4.4.7). For contractile activities below this threshold, interfaces become unstable to capillary wave fluctuations, leading to microphase separation. This demonstrates that the shape instability in Active Model H is fundamentally driven by capillary waves. This instability manifests through the growth of interface perturbations determined by the interplay between activity, friction and surface tension.

Through linear stability analysis, we derived the growth rate for interface perturbations eq. (4.4.9). Here we see how friction modifies the dispersion relation, bridging between the q^3 scaling characteristic of Active Model B in the high friction limit and the q scaling of standard Active Model H in the low friction regime. In the first case, capillary waves grow diffusively as in a dry system, while at low friction, hydrodynamic effects change the instability.

Furthermore, the most unstable mode scales as $q_{\max} \propto \sqrt{\Gamma}$ when the product ΓM is constant, which is a scaling behavior that persists across different parameter regimes.

Numerical simulations using pseudo-spectral methods validate our theoretical predictions. We verified the existence of the critical activity threshold across multiple parameter sets, confirmed the predicted scaling of the most unstable mode $q_{\max} \propto \sqrt{\Gamma}$ when maintaining constant ΓM, and observed the capillary wave-driven instability in interface evolution. Interestingly, linear analysis captures correctly the instability threshold but did not predict the behavior of the most unstable mode quantitatively; this is not surprising as our analysis is valid in the limit of small q and other mechanisms could contribute to the growth of capillary waves.

To extend our studies, one could further analyze what happens when forces that do not derive from a stress term are included in the dynamics. We expect that such non-stress forces, by breaking the $\phi \to -\phi$ symmetry, may drive the system into an active foam state, similar to [8], [23], where symmetry breaking leads to persistent network-like structures rather than droplet-like domains. Additionally, analyzing correlation functions and fluctuations in the presence of friction is central for understanding hydrodynamic effects, as it is still unclear whether in active systems, differently from passive ones, the large scale decay of correlations is impacted by the presence of fluid flows.

Bibliography

[1] A. Tiribocchi, R. Wittkowski, D. Marenduzzo, and M. E. Cates, "Active model h: Scalar active matter in a momentum-conserving fluid," *Physical review letters*, vol. 115, no. 18, p. 188 302, 2015.

[2] F. Caballero, A. Maitra, and C. Nardini, "Interface dynamics of wet active systems," *Physical Review Letters*, vol. 134, no. 8, p. 087 105, 2025.

[3] M. E. Cates and C. Nardini, "Active phase separation: New phenomenology from non-equilibrium physics," *Reports on Progress in Physics*, vol. 88, no. 5, p. 056 601, 2025.

[4] A. J. Bray, "Theory of phase-ordering kinetics," *Advances in Physics*, vol. 51, no. 2, pp. 481–587, 2002.

[5] P. C. Hohenberg and B. I. Halperin, "Theory of dynamic critical phenomena," *Reviews of Modern Physics*, vol. 49, no. 3, p. 435, 1977.

[6] S. Ramaswamy, "The mechanics and statistics of active matter," *Annu. Rev. Condens. Matter Phys.*, vol. 1, no. 1, pp. 323–345, 2010.

[7] E. Tjhung, C. Nardini, and M. E. Cates, "Cluster phases and bubbly phase separation in active fluids: Reversal of the ostwald process," *Physical Review X*, vol. 8, no. 3, p. 031 080, 2018.

[8] G. Fausti, E. Tjhung, M. Cates, and C. Nardini, "Capillary interfacial tension in active phase separation," *Physical review letters*, vol. 127, no. 6, p. 068 001, 2021.

[9] S. F. Banani, H. O. Lee, A. A. Hyman, and M. K. Rosen, "Biomolecular condensates: Organizers of cellular biochemistry," *Nature reviews Molecular cell biology*, vol. 18, no. 5, pp. 285–298, 2017.

[10] N. Ganai, S. Sengupta, and G. I. Menon, "Chromosome positioning from activity-based segregation," *Nucleic acids research*, vol. 42, no. 7, pp. 4145–4159, 2014.

[11] K. Siteur, Q.-X. Liu, V. Rottschäfer, *et al.*, "Phase-separation physics underlies new theory for the resilience of patchy ecosystems," *Proceedings of the National Academy of Sciences*, vol. 120, no. 2, e2202683120, 2023.

[12] R. Zakine, J. Garnier-Brun, A.-C. Becharat, and M. Benzaquen, "Socioeconomic agents as active matter in nonequilibrium sakoda-schelling models," *Physical Review E*, vol. 109, no. 4, p. 044 310, 2024.

[13] A. Doostmohammadi, S. P. Thampi, and J. M. Yeomans, "Defect-mediated morphologies in growing cell colonies," *Physical review letters*, vol. 117, no. 4, p. 048 102, 2016.

[14] T. Sanchez, D. T. Chen, S. J. DeCamp, M. Heymann, and Z. Dogic, "Spontaneous motion in hierarchically assembled active matter," *Nature*, vol. 491, no. 7424, pp. 431–434, 2012.

[15] E. Heller and E. Fuchs, "Tissue patterning and cellular mechanics," *Journal of Cell Biology*, vol. 211, no. 2, pp. 219–231, 2015.

[16] M. E. Cates and E. Tjhung, "Theories of binary fluid mixtures: From phase-separation kinetics to active emulsions," *Journal of Fluid Mechanics*, vol. 836, P1, 2018.

[17] P. G. Debenedetti, "Metastable liquids: Concepts and principles," 1996.

[18] R. Singh and M. Cates, "Hydrodynamically interrupted droplet growth in scalar active matter," *Physical review letters*, vol. 123, no. 14, p. 148 005, 2019.

[19] P. Galajda, J. Keymer, P. Chaikin, and R. Austin, "A wall of funnels concentrates swimming bacteria," *Journal of bacteriology*, vol. 189, no. 23, pp. 8704–8707, 2007.

[20] H. Diamant, "Hydrodynamic interaction in confined geometries," *Journal of the Physical Society of Japan*, vol. 78, no. 4, pp. 041 002–041 002, 2009.

[21] F. Caballero and M. C. Marchetti, "Activity-suppressed phase separation," *Physical Review Letters*, vol. 129, no. 26, p. 268 002, 2022.

[22] F. Caballero, "Cupss: A package for pseudo-spectral integration of stochastic pdes," *arXiv preprint arXiv:2405.02410*, 2024.

[23] P. Gulati, F. Caballero, and M. Cristina Marchetti, "Active fluids form system-spanning filamentary networks," *Physical Review Letters*, vol. 134, no. 13, p. 138 301, 2025.

A. Solution of Stokes equation with friction

We solve the Stokes equation with a friction term and a delta-like force:

$$0 = \eta \nabla^2 \mathbf{v} - \Gamma \mathbf{v} + \nabla P + F\delta(\mathbf{r}), \quad \nabla v = 0. \tag{A.0.1}$$

We start by defining

$$P = \frac{F \cdot \Pi}{8\pi\eta}, \quad v = \frac{G \cdot F}{8\pi\eta}$$

and using Einstein notation:

$$P = \frac{F_i \Pi_i}{8\pi\eta}, \quad v_i = \frac{G_{ij} F_j}{8\pi\eta},$$

where Π is a vector field and G is a tensor.
Next we Fourier transform eq. (A.0.1) and substituting the equations above

$$-\eta k^2 \hat{v} + \Gamma \hat{v} - ikP = -F, \tag{A.0.2}$$

$$-ik_i \frac{\hat{\Pi}_j F_j}{8\pi\eta} - k^2 \frac{\hat{G}_{ij}}{8\pi\eta} \eta F_j - \Gamma \frac{\hat{G}_{ij}}{8\pi\eta} F_j = -F_j \delta_{ij}, \tag{A.0.3}$$

$$-ik_i \frac{\hat{\Pi}_j}{8\pi\eta} - k^2 \frac{\hat{G}_{ij}}{8\pi\eta} \eta - \Gamma \frac{\hat{G}_{ij}}{8\pi\eta} = -\delta_{ij}. \tag{A.0.4}$$

The incompressibility equation in (A.0.1) reduces to $k_i \hat{G}_{ij} = 0$, so multiplying eq. (A.0.4) by k_i we get:

$$\frac{\hat{\Pi}_j}{8\pi\eta} = -i \frac{k_j}{k^2},$$

and substituting back in eq. (A.0.4), we find:

$$\frac{\hat{G}_{ij}}{8\pi\eta} = \frac{\delta_{ij}}{\eta k^2 + \Gamma} - \frac{k_i k_j}{k^2(\eta k^2 + \Gamma)}. \tag{A.0.5}$$

At this point it's a matter of finding the inverse Fourier transform.

In the main text, we need the Fourier transform only in **x** leaving the y component real, call this quantity $\mathcal{T}_{yj}(q, y)$.

First we look at $j = y$ in eq. (A.0.5) and setting $\lambda^2 = \Gamma/\eta$, $q^2 = k_x^2 + k_z^2$:

$$\begin{aligned}
\mathcal{T}_{yy}(q,y) &= \frac{1}{2\pi\eta}\int_{-\infty}^{\infty} dk_y \frac{1}{\lambda^2+q^2+k_y^2}\left(1-\frac{k_y^2}{k_y^2+q^2}\right)e^{ik_yy} = \\
&= \frac{1}{2\pi\eta}\int_{\infty}^{\infty} dk_y \frac{q^2 e^{ik_yy}}{(\lambda^2+q^2+k_y^2)(q^2+k_y^2)} = \\
&= \frac{q^2}{2\pi\eta}\int_{-\infty}^{\infty} dk_y \frac{1}{\lambda^2}\left(\frac{1}{k_y^2+q^2}-\frac{1}{k_y^2+\lambda^2+q^2}\right)e^{ik_yy} = \\
&= \frac{q^2}{2\Gamma}\left(\frac{e^{-|y|q}}{q}-\frac{e^{-|y|\sqrt{\lambda^2+q^2}}}{\sqrt{\lambda^2+q^2}}\right).
\end{aligned}$$

Evaluating in $y = 0$

$$\mathcal{T}_{yy}(q,0) = \frac{1}{2\Gamma}\left(q-\frac{q^2}{\sqrt{\lambda^2+q^2}}\right). \tag{A.0.6}$$

Then keeping $j \neq y$:

$$\begin{aligned}
\mathcal{T}_{yj}(q,y) &= -\frac{1}{2\pi\eta}\int_{-\infty}^{\infty} dk_y \frac{k_jk_ye^{ik_yy}}{(\lambda^2+q^2+k_y^2)(k_y^2+q^2)} = \\
&= -\frac{1}{2\pi\eta}\int_{-\infty}^{\infty} dk_y \frac{1}{\lambda^2}\left(\frac{1}{k_y^2+q^2}-\frac{1}{k_y^2+\lambda^2+q^2}\right)k_jk_ye^{ik_yy} = \\
&= -\frac{k_j i\,\mathrm{sgn}(y)}{2\Gamma}\left(e^{-|y|q}-e^{-|y|\sqrt{\lambda^2+q^2}}\right).
\end{aligned}$$

And evaluating in $y = 0$

$$\mathcal{T}_{yj}(q,0) = 0. \tag{A.0.7}$$

B. Linear Order approximation

The model is

$$\begin{cases} \partial_t\phi = -\nabla_i\phi \int d\bar{r}' G_{ij}(\bar{r}-\bar{r}') f_j(\bar{r}') + M\nabla^2\mu \\ \mu = \frac{\delta}{\delta\phi}\int d\bar{r}\left[f(\phi)+\frac{k}{2}|\nabla\phi|^2\right] = f'(\phi) - k\nabla^2\phi \end{cases} . \tag{B.0.1}$$

We substitute the ansatz for a flat interface eq. (4.3.1) and setting $u = y - h(\mathbf{x}, t)$ we get

$$\varphi'(u)\partial_t h + \nabla_i\varphi(u) \int d\mathbf{r}' G_{ij}(\mathbf{r}-\mathbf{r}') F_j(\mathbf{r}') = M\nabla^2\mu. \tag{B.0.2}$$

Now we want to obtain an approximation at the linear order.
Consider the density gradient term:

$$\nabla_y\varphi(u) = \varphi'(u), \quad \nabla_{\mathbf{x}}\varphi(u) = -\varphi'(u)\nabla_{\mathbf{x}}h(\mathbf{x},t), \tag{B.0.3}$$

where $\varphi'(u)$ denotes the derivative with respect to u.
If the integral factor at the lowest order contains gradients of $h(\mathbf{x}, t)$, then terms coming from $i = \mathbf{x}$ are non-linear and they will be discarded. We will see that this is indeed the case and only the contribution $i = y$ has linear terms.
Write the stress $\mathbf{F} = \mathbf{F}^{\text{grad}} + \mathbf{F}^{*}$, where $\mathbf{F}^{\text{grad}} = -\nabla_i\sigma_{ij}$ with $\sigma_{ij} = \tilde{k}\left[(\nabla_j\phi)(\nabla_i\phi) - \frac{1}{d}|\nabla\phi|^2\right]$ is the contribution coming from a gradient and $F_i^{*} = K_1\phi(\nabla_i\phi)(\nabla^2\phi) + K_2|\nabla\phi|^2\nabla_i\phi$ includes the higher order therms.
Along the y direction we have

$$\begin{aligned} -\frac{F_y^{\text{grad}}}{\tilde{k}} &= \nabla_i\sigma_{yj} = \nabla_i\left[(\nabla_y\varphi(u))(\nabla_i\varphi(u)) - \frac{\delta_{yi}}{d}|\nabla\varphi(u)|^2\right] = \\ &= \nabla_y\sigma_{yy} + \nabla_{\mathbf{x}}[\nabla_y\varphi(u)\nabla_{\mathbf{x}}\varphi(u)] = \\ &= \nabla_y(\varphi'(u))^2 - \frac{1}{d}\nabla_y[(\varphi'(u))^2(1+|\nabla_x h(\mathbf{x},t)|^2) + \\ &\qquad - \nabla_{\mathbf{x}}[\varphi'(u)\times\varphi'(u)\nabla_{\mathbf{x}}h(\mathbf{x},t)] = \\ &= 2\varphi'(u)\varphi''(u) - \frac{2}{d}\varphi'(u)\varphi''(u)(1+|\nabla_x h(\mathbf{x},t)|^2) + \\ &\qquad + 2\varphi'(u)\varphi''(u)|\nabla_{\mathbf{x}}h(\mathbf{x},t)|^2 - (\varphi'(u))^2\nabla_{\mathbf{x}}^2 h(\mathbf{x},t). \end{aligned}$$

Then keeping only the linear terms we get

$$F_y^{\text{grad}} = -\tilde{k}\left[2\frac{(d-1)}{d}\varphi'(u)\varphi''(u) - (\varphi'(u))^2\nabla_{\mathbf{x}}^2 h(\mathbf{x},t)\right].$$

Similarly keeping the linear terms in the higher order part we find

$$F_y^* = K_1\varphi\varphi'\varphi'' + K_1\varphi(\varphi')^2\nabla_{\mathbf{x}}^2 h(\mathbf{x},t) + K_2\partial_u(\varphi')^3 \tag{B.0.4}$$

where we can ignore the term without h as they account for pressure jumps across the interface.
The stress along $\mathbf{x}$ gives:

$$-\frac{F_{\mathbf{x}}^{\text{grad}}}{\tilde{k}} = \nabla_y\sigma_{\mathbf{x}y} + \nabla_{\mathbf{x}}\sigma_{\mathbf{x}\mathbf{x}},$$

the first term is computed above and the second leads only to non-linear terms, then linearizing

$$F_{\mathbf{x}}^{\text{grad}} = \tilde{k}(\varphi'(u))^2\nabla_{\mathbf{x}}^2 h(\mathbf{x},t). \tag{B.0.5}$$

For the other term at the linear order

$$F_{\mathbf{x}}^* = -K_1\varphi\varphi'\varphi''\nabla_{\mathbf{x}} h(\mathbf{x},t) - K_2(\varphi')^3\nabla_{\mathbf{x}} h(\mathbf{x},t). \tag{B.0.6}$$

$F_{\mathbf{x}}$ contains all terms with some function of the gradient $\nabla_{\mathbf{x}} h(\mathbf{x},t)$ and, when multiplied with the φ expansion in eq. (B.0.3), only $i = y$ in eq. (B.0.1) leads to linear terms.

Finally we turn to the modified Oseen tensor and note that in the sharp interface limit, the stress is located at the interface and $G_{ij}(\mathbf{r}-\mathbf{r}') \approx G_{ij}(\mathbf{x}-\mathbf{x}', \mathbf{y} - h(\mathbf{x},t))$. Expanding this quantity in the second argument, the only term without gradients in $h(\mathbf{x},t)$ is $G_{ij}(\mathbf{x}-\mathbf{x}',0)$. The contribution from $G_{\mathbf{x}y}(\mathbf{x}-\mathbf{x}',0)$ turns out to be zero (cfr. eq. (A.0.7)).
Combining everything, eq. (B.0.1) at linear order is

$$\begin{aligned}\varphi'(u)\partial_t h - \varphi'(u)\int d\mathbf{x}'dy'\, G_{yy}(\mathbf{x}-\mathbf{x}',0)[\tilde{k}\nabla_{y'}\sigma_{yy} - \tilde{k}(\varphi')^2\nabla_{\mathbf{x}'}^2 h(\mathbf{x}',t) - K_1\varphi(\varphi')^2\nabla_{\mathbf{x}'} h(\mathbf{x}',t)] = \\ = M\nabla^2\mu,\end{aligned} \tag{B.0.7}$$

The integral in y containing $\nabla_y\sigma_{yy}$ and $\varphi(\varphi')^2$ evaluate to zero, then

$$\varphi'(u)\partial_t h + \tilde{k}\varphi'(u)\int d\mathbf{x}'dy'\, G_{yy}(\mathbf{x}-\mathbf{x}',0)(\varphi'(u'))^2\nabla_{\mathbf{x}'}^2 h(\mathbf{x}',t) = M\nabla^2\mu, \tag{B.0.8}$$

To properly account for the right hand side contribution, we need to invert the Laplacian in the chemical potential μ.

For a function $s(\bar{r}) = \nabla^2 g(\bar{r})$, the Fourier transform in the directions **x**, orthogonal to y, gives:

$$\hat{s}(q,y) = (\partial_y^2 - |q|^2)\hat{g}(q,y),$$

with the associated Green's function $L_q(y-y_1) = \frac{1}{2q}e^{-q|y-y_1|}$, yielding:

$$\hat{g}(q,y) = \int dy_1\, L_q(y-y_1)\hat{s}(q,y_1) = \int dy_1\, \frac{1}{2q}e^{-q|y-y_1|}\hat{s}(q,y_1). \tag{B.0.9}$$

Applying this method, we are able to invert the laplacian in eq. (B.0.8):

$$\begin{aligned}\nabla^{-2}\left[\varphi'(u)\partial_t h + \frac{\tilde{k}}{k}\sigma_{eq}\varphi'(u)\int d\bar{r}' G_{yy}(\bar{x}-\bar{x}',0)\nabla_x^2 h(\bar{x}',t)\right] &= \\ = M\Delta f + Mk(\varphi''(u) + \varphi'(u)\nabla_{\mathbf{x}}^2 h(\mathbf{x},t)),\end{aligned}$$

where we expanded $\nabla^2\varphi(u)$ using eq. (4.3.1) and $\sigma_{\mathrm{eq}} = k\int(\varphi')^2 dy$ is the equilibrium surface tension eq. (2.2.3).
After taking the Fourier transform in **x** using equation (B.0.9), multiplying by $\varphi'(u)$ and integrating over y, we arrive at

$$\int dy \int dy_1\, \frac{1}{2q}e^{-q|y-y_1|}\varphi'(u)\varphi'(u_1)\left[\partial_t h_q - \frac{\tilde{k}}{k}\sigma_{eq}q^2\mathcal{T}_{yy}(q,0)h_q\right] = M\Delta f\,\delta(q) - M\sigma_{eq}q^2 h_q,$$

and finally, isolating $\partial_t h_q$:

$$\partial_t h_q = -\sigma_{\mathrm{eq}}q^2\left[\frac{\tilde{k}}{k}\mathcal{T}_{yy}(q,0) + \frac{2Mq}{A_{\mathrm{eq}}(q)}\right]h_q. \tag{B.0.10}$$

Where we defined $A_{\mathrm{eq}}(q) = \int dy\,dy_1\, e^{-q|y-y_1|}\varphi'(u)\varphi'(u_1)$ and the function $\mathcal{T}_{yy}(q,0)$ is the transformed Oseen tensor eq. (A.0.6):

$$\mathcal{T}_{yy}(q,0) = \frac{1}{2\Gamma}\left(q - \frac{q^2}{\sqrt{\lambda^2+q^2}}\right), \quad \text{with } \lambda^2 = \Gamma/\eta.$$

C. Summary of instability simulations

Below a comprehensive figure showing simulations at different friction Γ and mobility M, compared with the predicted instability criteria.
Highlighted in green is the stability treshold found by ,inear analysis in chapter 4.

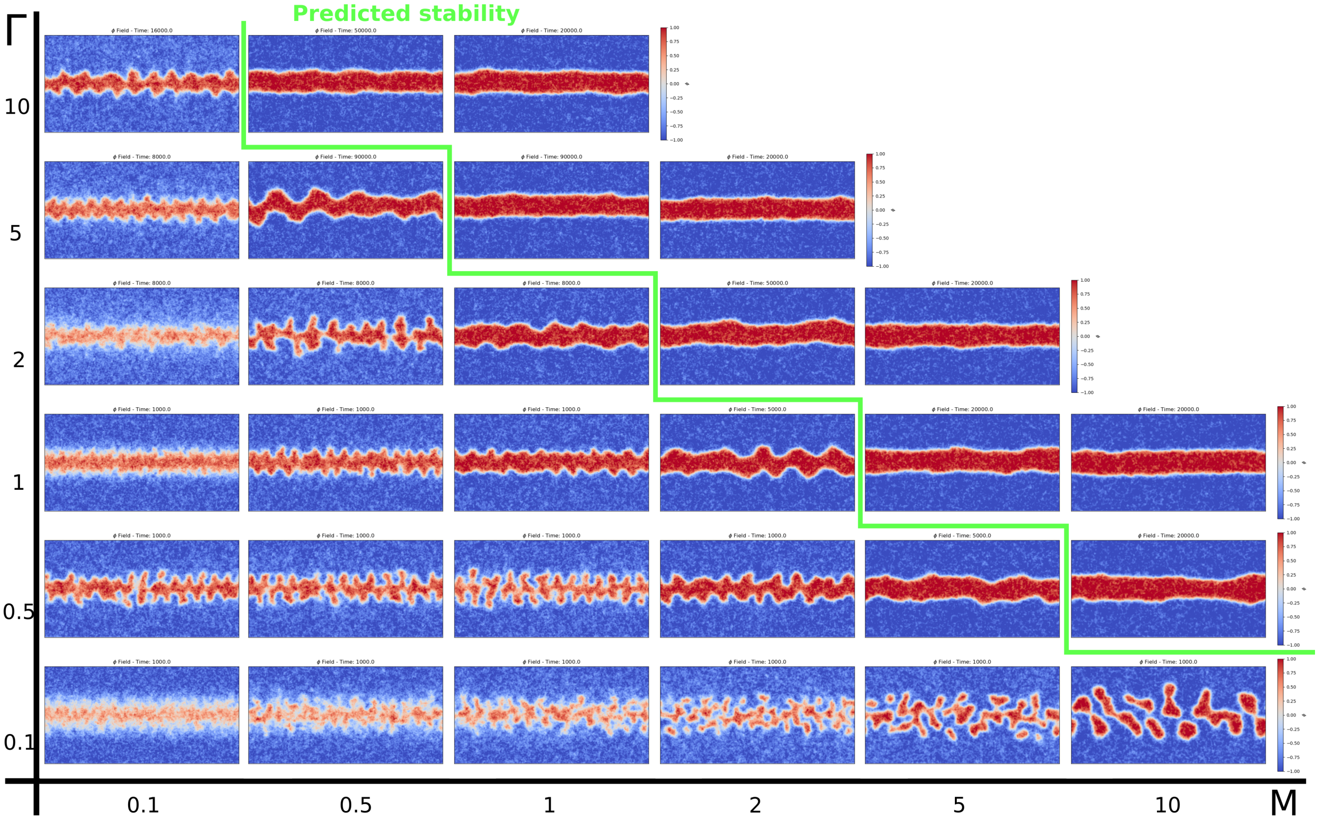

Figure C.1: Parameters values are: $a = 0 - .25$, $b = 0.25$, $k = 1$, $\tilde{k} = -4$, $M = 1$, $\eta = 1$ and $D = 0.005$.